A magnetotactic bacterium capable of magnetic sensing

Emilie Gachon, Sascha Lambert, Sandrine Grosse, Elsa Turrini, Emma Ropion, Stefan Klumpp, Christopher T. Lefèvre, Mila Sirinelli, Damien Faivre

iScience

Article

A magnetotactic bacterium capable of magnetic sensing

Graphical abstract

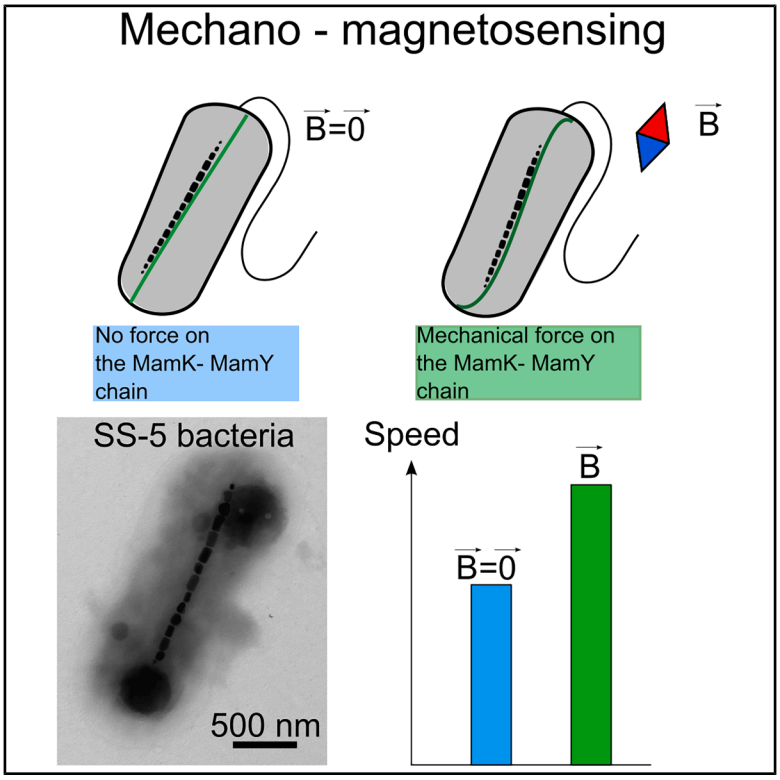

Highlights

- SS-5 magnetotactic bacteria (MTB) adapt their swimming speeds to magnetic field intensities
- Magnetic field intensities do not influence bacterial flagellar motion rotation
- Magnetosensing stems from magnetomechanical signal transduction via the magnetosome chain

Authors

Emilie Gachon, Sascha Lambert, Sandrine Grosse, ..., Christopher T. Lefèvre, Mila Sirinelli, Damien Faivre

Correspondence

emilie.gachon@cea.fr (E.G.), damien.faivre@cea.fr (D.F.)

In brief

Microbiology; Evolutionary biology

Gachon et al., 2025, iScience *28*, 113377
September 19, 2025
https://doi.org/10.1016/j.isci.2025.113377

CellPress

iScience

CellPress
OPEN ACCESS

Article

A magnetotactic bacterium capable of magnetic sensing

Emilie Gachon,[1,3,*] Sascha Lambert,[2] Sandrine Grosse,[1] Elsa Turrini,[1] Emma Ropion,[1] Stefan Klumpp,[2] Christopher T. Lefèvre,[1] Mila Sirinelli,[1] and Damien Faivre[1,*]

[1]Aix Marseille Université, CEA, CNRS, BIAM, 13115 Saint-Paul-Lez-Durance, France

[2]University of Göttingen, Institute for the Dynamics of Complex Systems, Friedrich-Hund-Platz 1, 37077 Göttingen, Germany

[3]Lead contact

*Correspondence: emilie.gachon@cea.fr (E.G.), damien.faivre@cea.fr (D.F.)

https://doi.org/10.1016/j.isci.2025.113377

SUMMARY

Magnetosensitive organisms have the ability to sense and respond actively to features of magnetic fields such as the direction or magnitude. Until now, magnetosensing has been characterized primarily in higher organisms, involving either a cryptochrome-based mechanism or direct magnetic interactions with magnetic particles. Magnetotactic bacteria, microorganisms forming intracellular chains of magnetic nanoparticles, are thought to only passively orient along field lines. In this study, we reveal that the cultivated magnetotactic bacterium SS-5 also exhibits magnetosensing. The microorganisms indeed swim faster in a physiological magnetic field compared to when the field is canceled. This speed difference is independent of illumination wavelength but is altered when the bacterial magnetic backbone is disrupted. We thus propose that magnetosensing in the bacteria originates from a magnetomechanical signal transduction along the magnetotactic filament. Our findings also show that this response depends on relative changes in magnetic field intensity, akin to the Weber-Fechner laws, suggesting that magnetosensing operates similarly to other forms of taxes.

INTRODUCTION

In recent years, the impact of magnetic fields on living organisms has garnered significant attention from chemists, zoologists, physicists, and biologists.[1–4] Evidence indicates that vertebrates, invertebrates, and certain bacteria utilize the geomagnetic field (GMF) for migration,[1,2,5] body alignment,[6–8] and locating nutrients or habitats.[9–11] Magnetosensing, the ability to sense or modify one's behavior based on magnetic field strength or direction, has been documented only in higher organisms like vertebrates and mollusks. Migrating birds, for example, use a photo-initiated quantum process in retinal cryptochrome flavoproteins to map the Earth's magnetic field.[12–16] Studies initially suggested that ferromagnetic crystals in their beaks were used to sense magnetic field strength.[17] However, recent studies have casted some doubts on the validity of these studies by showing that the clusters of iron-rich cells in the upper beak of pigeons are actually most likely macrophages and not magnetosensitive neurons and that instead, a vision-mediated mechanism underlies the magnetic compass in migratory birds.[18,19] Sea turtles, however, exhibit light-independent magnetic orientation, suggesting an iron-based molecular sensor.[20] Initially, *Caenorhabditis elegans* nematode were also thought to perform magnetic orientation via an iron-based molecular sensor.[21] Since then however, *C. elegans* have been proven to not be robust model organisms for magnetic sensing.[22] Thus, magnetosensing is debated in terms of not only mechanisms but also organisms.

Conversely, magnetotactic bacteria (MTB) passively align with the Earth's magnetic field lines by using an intracellular chain of ferromagnetic crystals surrounded by a lipid bilayer, known as the magnetosome chain, aiding their migration toward micro-oxic or anoxic environments.[9,10,23,24] This passive alignment, combined with active aerotaxis toward their preferred low-oxygen environments, is termed magneto-aerotaxis.[6] Genetic investigations have started to uncover the molecular interactions at play in magneto-aerotaxis, in particular highlighting the role of the particular gene operon called *Cheop1* in their aerotactic behavior.[25] Potential active magnetosensing involving molecular components have been proposed, in particular a methyl-accepting chemetoaxis protein was shown to be involved in the cell's ability to sense the angle between the cells' orientation and that of the magnetic field.[26] Yet, the current paradigm in MTB research is that cells do not actively sense magnetic fields and only passively align along field lines.

We tracked hundreds of the spirilla, bi-flagellated *Magnetospirillum gryphiswaldense*, MSR-1, and of the rod-shaped, mono-flagellated Gammaproteobacteria SS-5 when the GMF is canceled and in the presence of additional external magnetic fields ranging from 50 μT (physiological field) to 2 mT[27] to test their swimming response to the presence of an external magnetic field.

While the typical passive orientation of the cell body is observed for MSR-1, we demonstrate an active response of the SS-5's swimming speeds to a magnetic field and hence

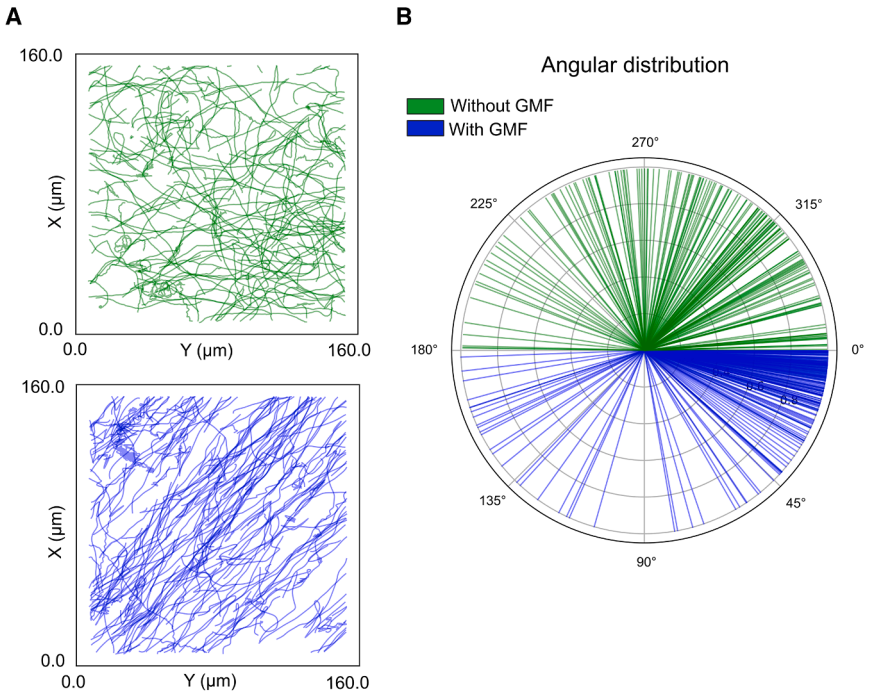

Figure 1. Trajectories of SS-5 bacteria in the presence and absence of the Earth's magnetic field

(A) 2D trajectories of individual cells in the presence and absence of a GMF.

(B) Angular distribution of the direction of the trajectories with respect to the South magnetic pole.

that this species is capable of magnetosensing. We demonstrate that the underlying physical mechanism of magnetosensing involves the transmission of a magnetomechanical signal along the magnetosome filament, coupled with the logarithmic dependence of SS-5's bacterial flagellar motor rotational speed on magnetic field intensity. This relationship is reminiscent of the Weber-Fechner laws, which are commonly used to describe other sensory mechanisms, such as chemotaxis. Our results indicate that MTB, particularly SS-5, have evolved to optimize their swimming behavior in weak magnetic fields, providing a distinct advantage in the dynamic chemical environments of their aquatic habitats.

RESULTS

SS-5 explores more space in the presence of a geomagnetic field

SS-5 bacteria were tracked in the presence and absence of a GMF. The GMF at the location of our institute was measured to be of 46.9 μT with a 40.5 μT downward vertical component, a 23.7 μT horizontal component pointing toward the geographical north, and a 1.08 μT horizontal component pointing toward the East.

Figure 1A shows that the two-dimensional (2D) projections of the 3D trajectories of SS-5 in the presence of a GMF are more aligned and ordered than those of the bacteria swimming in the absence of a GMF (when the Earth's magnetic field is compensated for). Figure 1B shows the angular distribution of all the trajectories recorded and analyzed. The average angle, α, of the 2D projections of the 3D trajectories with the south magnetic pole in the presence of a GMF is of $\alpha = 16.8^{\circ} \pm 0.1$, whereas in the absence of a GMF it is of $a = 66.11^{\circ} \pm 0.2$.

SS-5 bacteria use their single polar flagella as a propeller. Lacking other flagella, they explore their space using the "run-reverse" mechanism, where, when the bacterial flagellar motor rotates counter-clockwise (CCW) the cell body is pushed forward. When the motor rotates clock-wise (CW) the flagella pull the bacteria backward and the bacteria's trajectory shows a characteristic 180° angle reversal. When transitioning from a run to a reverse, the bacteria's speed drops very suddenly to values close to 0 $\mu m s^{-1}$. By counting these drops in the speed traces, we studied the differences induced by the presence of a magnetic field in the switching rate, $\bar{s}$, between runs and reversals of SS-5 bacteria. In the presence of a GMF, SS-5 bacteria performed very long runs with very few switching event, $\bar{s} = 0.35 \pm 0.12\, s^{-1}$. In contrast, SS-5 bacteria had less directional movements and performed on average, $\bar{s} = 3.57 \pm 0.86\, s^{-1}$ in the absence of a GMF.

SS-5's swimming speed is tuned by magnetic fields

SS-5 bacteria were tracked in three dimensions in different homogeneous oxygen environments and in the presence of different magnetic field intensities. The sample was imaged under a 585-nm LED illumination because it is unlikely to interact with potential phytochromes (often sensitive to red light) or cryptochromes (sensitive to blue light), which could potentially be present in SS-5 bacteria. Figure 2 shows that SS-5 bacteria swim approximately 1.5 times faster in the presence of the GMF than those swimming in the same media but when the GMF is canceled.

The trajectories of most bacteria are helical, driven by the rotation of the cell body by the rotary motor. While this is likely true for SS-5 as well, no helical trajectories were observed at our resolution. This may be attributed to the geometry of SS-5's cell body and its single-flagellum propulsion system. Additionally, the presence of a GMF likely accentuates this effect by constraining the cell's movement to a more linear trajectory. Consequently, the trajectory speeds reported in this study represent the average absolute speed measured between consecutive frames.

The speed of SS-5 continues to increase and reaches a roughly 60% increase in speed for fields up to 150 μT. For larger field strengths, up to 2 mT, the bacteria's speed decreases and plateaus at roughly 1.4 times that of bacteria in the absence of an external magnetic field. SS-5 bacteria naturally perform

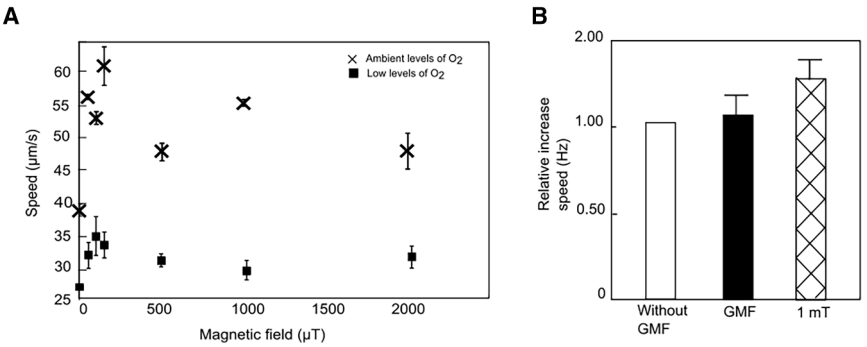

Figure 2. SS-5 swimming speed as a function of magnetic field intensity and oxygen concentration

(A) The average 3D speed of SS-5 bacteria imaged under a 585 nm illumination and measured in low oxygen concentrations (in media flushed with nitrogen for 10 min prior to imaging) and ambient oxygen concentrations increases in the presence of the Earth's magnetic field and with increasing fields up to 150 μT before decreasing and plateauing for fields from 500 μT up to 3 mT. At least 50 cells were tracked per data point, and the error bars correspond to the standard error of the average speed of all the analyzed cells' trajectories. From 0 mT to 3 mT, the average speed of bacteria swimming in ambient oxygen concentrations of oxygen are 38.7 ± 1.0 μm/s, 56.4 ± 0.4 μm/s, 53.1 ± 1.0 μm/s, 61.1 ± 2.9 μm/s, 47.8 ± 1.3 μm/s, 55.4 ± 0.7 μm/s, 48.1 ± 2.7 μm/s and 25.9 ± 2.0 μm/s, 30.9 ± 2.0 μm/s, 33.9 ± 2.0 μm/s, 32.4 ± 2.0 μm/s, 30.5 ± 1.0 μm/s, 28.9 ± 1.5 μm/s, and 30.9 ± 1.8 μm/s for bacteria in low oxygen concentrations.

(B) Effect of different magnetic field intensities on SS-5's bacterial flagellar motor's rotational speed. Speeds were normalized with respect to the speed of the average speed of the bacterial flagellar motor in the absence of a GMF (without a GMF: 1.43 ± 0.2; 1 mT: 1.71 ± 0.1). Student's t tests revealed no statistical differences for the bacterial flagellar motor's rotational speed in the presence and absence of a GMF (p value of 0.39), whereas a p value of 0.003 was obtained when comparing the speed of the bacterial flagellar motors in the absence of a GMF and with an external magnetic field of 1 mT. A p value of 0.02 was obtained when comparing the rotation of the bacterial flagellar motor in the presence of a GMF and a field 1 mT.

magneto-aerotaxis to migrate toward low oxygen concentrations. Hence, bacteria in ambient oxygen conditions and bacteria in lower oxygen concentrations (bacteria exposed to nitrogen for 10 min prior to imaging) were tracked separately and compared. Figure 2 shows that cells in low oxygen environments naturally swim slower than when they are in their less-preferred oxic environments despite the presence or absence of any external magnetic field. However, similarly to cells in oxic conditions, cells in micro-oxic environments swim up to 1.4 times faster with increasing fields up to 150 μT. Their 3D speed then decreases and plateaus for greater fields up to 2 mT at 1.1 times the speed of the bacteria in the absence of any external magnetic fields.

To test whether these variations in speed could be attributed to changes in the rotational speed of the bacterial flagellar motor under the influence of different external magnetic fields, SS-5 bacteria were tethered by their flagellum to a glass microscope slide by letting the cells sediment in the presence of a 1 mT z-field. Once anchored, the cell body rotates, powered by the rotational motor. By imaging and tracking the position of the cell body, the rotational speed of the motor can be monitored under the influence of different stimuli. Figure S1 shows that the counter-clockwise rotational speed of the bacterial flagellar motor is only significantly increased when cells are exposed to high magnetic fields. A Student's t test between the motor's rotational speeds in the absence and presence of a GMF yielded a p value of 0.39, whereas a p value of $p = 3 \times 10^{-3}$ was obtained when comparing the motor's rotational speeds in the absence of a GMF and in the presence of a 1 mT z-field.

Figure 2 shows that in the case of ambient levels of oxygen, the relative increase in speed between bacteria swimming in the absence of a GMF and in the presence of weak magnetic fields is of 1.4 ± 0.1. This relative increase in speed (the swimming speed in the presence of the Earth's magnetic field with respect to when the Earth's magnetic field is canceled) is greater than the relative increase of the bacterial flagellar motor's rotational speed for the same magnetic field intensities (Figure 2B). For greater fields of 1 mT, the relative 3D speed increase is of 1.4 ± 0.1, which matches that of the relative rotational speed increase of bacterial flagellar motors for strong fields (Figure 2B). In the sections described below, experiments using both weak and strong magnetic fields were thus conducted to probe and characterize the magnetosensing mechanism of SS-5.

Bacteria often swim along helical paths rather than on straight lines. If SS-5 swims helically, a magnetic field should straighten the helical path and reduce the swaying of the bacterium, which would result in an apparent increase in speed. To test whether the observed increase in speed results from a reduction of swaying, which we do not detect in the experimental trajectories, we turned to computer simulations. We simulated the swimming of SS-5 with an active Brownian particle equipped with a magnetic moment and driven by a rotating force describing propulsion by the flagellum.[28] The torques produced by the propulsion lead to helical trajectories. We sample these trajectories with the same resolution as the experimental data (at which the helicity may become undetectable; Figure S1 in the supporting information PDF) and extract the speed in the same way as from the experiments.

We determined plausible model parameters from the experimental trajectories using a Bayesian analysis. Simulations result in the angular distributions shown in Figure 3A agree with the experimental distributions. This analysis also provides the most plausible value for the magnetic moment of an SS-5 cell, which is found to be 9.4×10^{-16} Am^2 (95% credible interval [6.0, 12.8] 10^{-16} Am^2). We then simulated swimming in magnetic fields of 0 μT, 46.9 μT (geomagnetic field), and 150 μT and determined the speed. The results, depicted in Figures 3B–3D, show no increase in speed, indicating that the reduction of swaying is not sufficient to explain the speed increase due to the magnetic field seen in the experimental trajectories. The obtained magnetic moment is consistent with the measured values reported for other magnetotactic bacteria. It is important to emphasize that different measurement techniques can yield varying results. For instance, studies have reported magnetic moments ranging

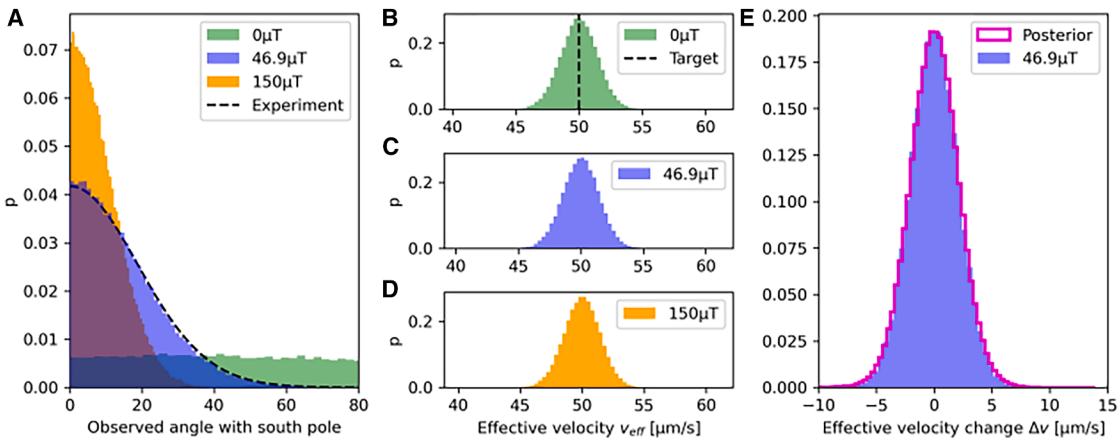

Figure 3. Numerical study on the effect of a magnetic field on the effective swimming speed of a simulated swimmer undergoing helical movement

(A) Distribution of the angle between the trajectory segments and the magnetic field lines. Depicted are the results for parameters that maximize the likelihood of the experimental distribution (MLE): a dipole moment of 9.4×10^{-16} Am^2, a swimmer radius of 0.9 μm, and a force angle of 45°. The latter parameter controls the helicity of the trajectory. The motor frequency was set to 200 Hz.

(B–D) Distribution of effective velocities as measured from 40 Hz snapshots from the simulation. It is unaffected by turning on the magnetic field. The propulsion velocity of the swimmer is tuned such that an effective velocity of 50 μm/s without a magnetic field is obtained using the MLE parameters.

(E) The distribution of observable changes in velocity by comparing two trajectories with and without a magnetic field. Depicted is the histogram of samples at the geomagnetic field strength using the MLE parameters. The posterior predictive of the velocity change is indicated by the magenta outline. It integrates the change in velocity over the entire plausible parameter space that is compatible with the experimental trajectories.

from $2.0 \pm 0.6 \times 10^{-16}$ Am^2[29] to 43×10^{-16} Am^2[30] for the MSR-1 strain, while values between 1 and 8×10^{-16} Am^2 have been reported for the AMB-1 strain.[31]

To confirm this more systematically, the Bayesian analysis probed the entire range of plausible parameters and again found no increase in speed due to reduced swaying (Figure 3E). As a control, we finally tested a much stronger field of B = 1,500 μT on a swimmer of size R = 0.4 μm with a reduced motor frequency of f = 50 Hz, which increases the swaying due to rotational movement. Here, the simulations showed an increase in speed as the helical trajectories were straightened out, but even then, the increase is much smaller than what is experimentally observed (shown in the supporting information PDF, Figures S4 and S5).

The radical pair mechanism is not at play

Weak magnetic fields have been shown to influence the outcome of a group of biochemical reactions involving radical pairs.[32–34]

A group of blue-light-sensitive photoreceptive proteins called cryptochromes is attracting a growing interest in this context.[35,36]

The analysis of SS-5's genome has revealed the presence of an open reading frame coding for a 475 amino acid protein presenting about 30% identity with bacterial proteins belonging to the photolyase/cryptochrome family. Therefore, to test this so-called radical-pair mechanism, the experiment presented in Figure 2 was repeated under different illumination (λ = 470 nm and λ = 635 nm); 635-nm LED illumination was used as an additional control to the experiment conducted under 585-nm LED-illumination to test whether any particular behavior occurred under blue-light illumination that could not be observed for any other wavelengths. Figure 3 shows the 3D speed of the same bacterial suspension under blue and red light as a function of the applied magnetic field. Although the absolute speed of the bacteria vary slightly, when performing a Student's t test, there is no statistical difference between the two datasets shown in Figure 4 (p value = 0.49), and the trend observed in Figure 2 remains under blue and red light illumination.

Cells with modified magnetosome organization are impaired

To test whether the magnetosomes and the magnetosome filament, which anchors the magnetosomes in chains, are involved in the increase of swimming speeds, bacteria, which produced few or no magnetosomes at all, and bacteria with plastically deformed magnetosome chains were tracked in three dimensions in the absence and in the presence of different magnetic fields. Transmission electron microscopy (TEM) images revealed an heterogeneous cell population in terms of magnetosome number for bacteria grown with traces of iron (1.8 μM vs. 31.8 μM used routinely in the growth medium). Some cells produced very few and small magnetosomes, which either formed short chains or were randomly dispersed inside the cell body (Figure 5D). Some cells did not present any magnetosomes (Figure 5C). When tracking bacteria from this diverse bacterial population in the presence of the GMF under oxic conditions, bacteria only swim 17% faster as opposed to when the GMF is canceled, compared to a 50% increase when the cells are grown in standard growth media (Figure 2).

Magnetosomes are positioned in the cell and maintained in place by an actin-like protein filament made up of MamK and MamJ proteins.[37] Following an established protocol,[38] we mechanically deformed or broke the magnetosome chains of SS-5. TEM imaging of bacteria grown in standard growth media

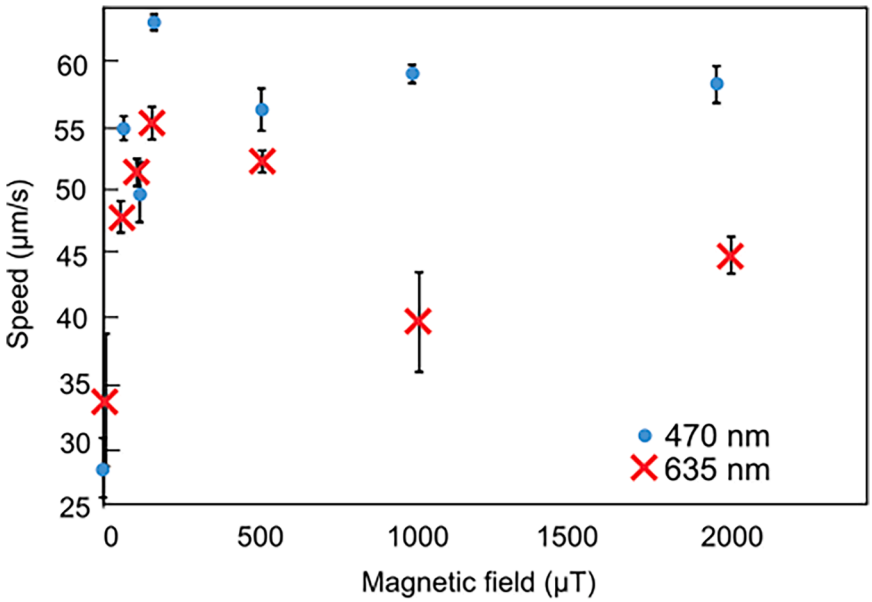

Figure 4. Effect of illumination wavelength on SS-5's swimming speed

The average 3D speed of SS-5 bacteria imaged under a 470 nm and 635 nm illumination increases in the presence of the Earth's magnetic field and with increasing fields up to 120 μT before decreasing and plateauing for fields from 500 μT up to 3 mT. At least 50 cells were tracked per data point, and the error bars correspond to the standard error of the average speed of all the cells' trajectories. The speeds of bacteria swimming under blue light illumination for speeds ranging from 0 mT to 3 mT are 28.7 ± 1.4 μm/s, 55.2 ± 0.9 μm/s, 50.1 ± 2.3 μm/s, 63.7 ± 0.5 μm/s, 56.7 ± 1.8 μm/s, 59.5 ± 0.8 μm/s, and 60.7 ± 1.5 μm/s. The speeds of bacteria swimming under red light illumination for speeds ranging from 0 mT to 3 mT are 34.6 ± 4.6 μm/s, 48.7 ± 1.3 μm/s, 52.2 ± 1.1 μm/s, 55.9 ± 1.3 μm/s, 53.0 ± 0.9 μm/s, 40.7 ± 3.8 μm/s, and 45.9 ± 1.4 μm/s.

and exposed to the magnetomechanical treatment yielded three sub-populations: a large population of cells with intact magnetosome chains, cells with deformed chains, and very few cells with broken chains. Once the cells were resuspended in liquid media, they were imaged and tracked in the presence or absence of a GMF. In the absence of the GMF, cells swim slower and the speed distribution is unimodal (Hartigan's dip test p value is equal to 0.9). In turn, the speed distribution becomes bimodal in the presence of a GMF with a Hartigan's dip test p value of 0.005 (Figure 5G). This holds true when doing empirical bootstrapping on 1,000 samples and a significance value of 0.1.

The motors' switching rates is dependent on magnetic field intensity fold changes

Tethered-cell assays were performed on SS-5 bacteria in the presence of an externally applied magnetic field. The absolute value of the magnetic field was changed after 60 s of imaging by either a 2-fold or a 10-fold increase spanning a magnetic field range of either 40 μT–1280 μT in the case of a 2-fold increase or a range of 10 μT–1000 μT in the case of a 10-fold increase. In the case of a 2-fold field relative increase, the average number of switching events between clockwise and counter-clockwise rotation of the bacterial flagellar motor is of 0.79 ± 0.19 compared to 1.09 ± 0.25 in the 10-fold relative increase case. The statistical analysis comparing these two groups revealed a p value of 0.008, indicating that different fold changes in magnetic fields influences the rate at which the bacterial flagellar motor switches between CCW and CW rotation.

DISCUSSION

The trajectories in Figure 1A show that in oxic environments and in the presence of a GMF, SS-5 bacteria have a natural tendency to swim toward the south magnetic pole and that canceling the GMF leads to a random swimming orientation. MTB in the Northern hemisphere are called North seekers because they tend to swim toward the geomagnetic South pole, the geographic North pole, in an oxygen-depleted gradient. However, in contrast to the findings presented in Figure 1, a preferential direction of swimming toward a specific magnetic pole under homogeneous oxygen concentrations has not been reported so far. Figure 2 shows a significant increase in the bacteria's swimming speeds in the presence of weak magnetic fields. Simulations showed that the straightening out of the trajectories and the lesser swaying of the bacteria as it swims in the presence of a geomagnetic field does not result in an increase in their swimming speed. For greater fields, the increase in swimming speeds is far less than what was measured experimentally. Additionally, magnetic fields between 50 μT and 150 μT lack the strength to restrict bacteria to uni-dimensional-like trajectories as depicted in Figure 1A.[23] The magnetic moment calculated from our trajectories is of 9.4×10^{-16} A.m^2. When considering the Langevin function, bacteria with such magnetic moments in the presence of the magnetic fields used in this study, are expected to have an average alignment of the cells to the magnetic field lines of 36.8°,[23] which is far less aligned than what is observed in our data (Figure 1).

Studies on MSR-1, which are reported to possess similar magnetic moments, have demonstrated that physiologically relevant magnetic fields optimize cellular throughput when swimming through sediment-mimicking microfluidic channels. In these conditions, cells efficiently travel from one end of the channel to the other. Stronger magnetic fields, however, hinder swimming by confining cells to magnetic field lines, making them susceptible to trapping in dents formed by the sediment's geometry. Conversely, in the absence of a magnetic field, cells exhibit random swimming patterns with reduced efficiency. Physiological fields strike a balance, providing a directional cue while remaining weak enough to allow cells to deviate from field lines and escape potential traps.

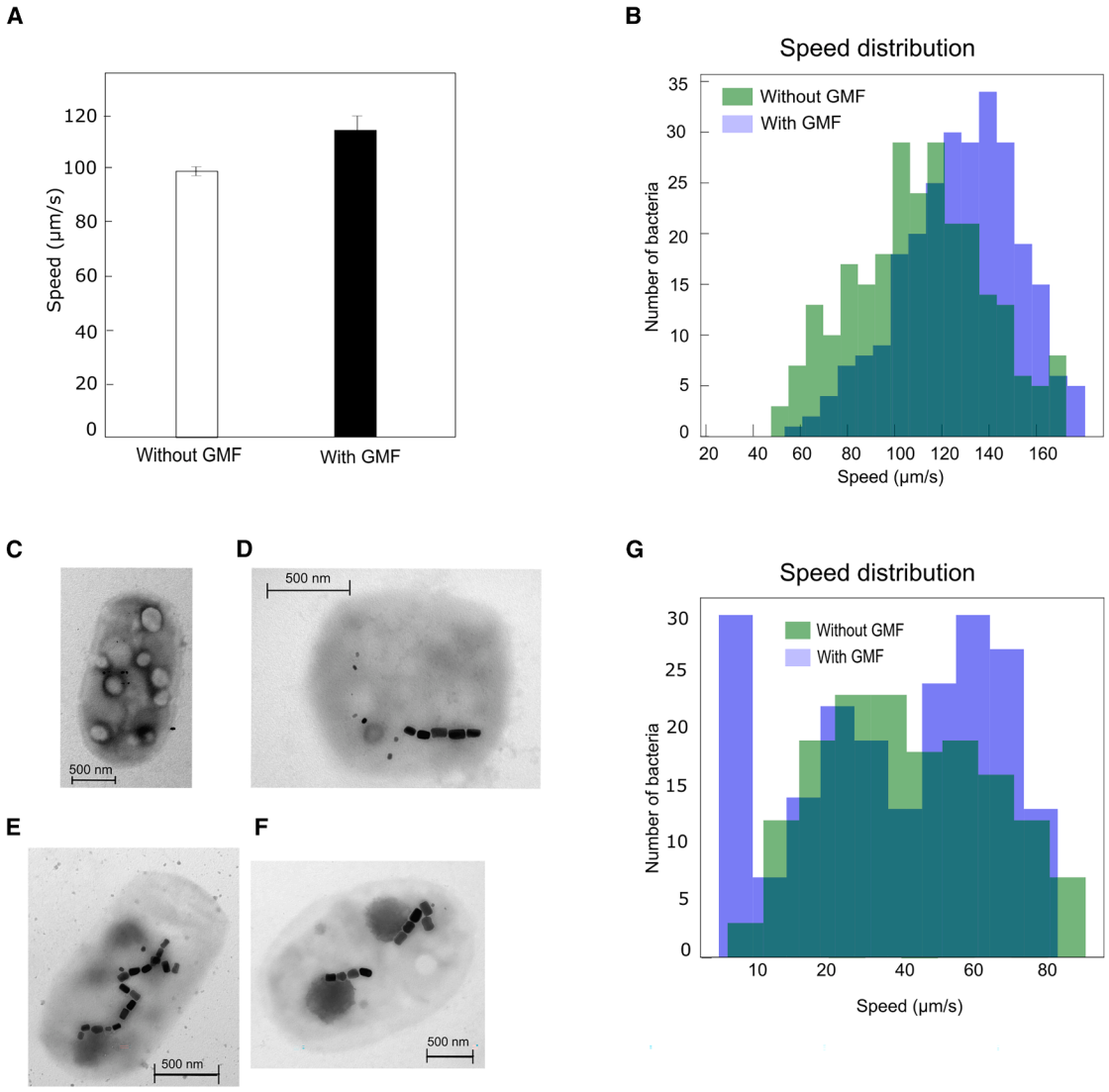

Figure 5. SS-5 bacteria with modified magnetosome chains

(A) Average speed of 262 bacteria with no or few magnetosomes in the presence of GMF and with the GMF compensated for (*t* value: −7.7 ; *p* value: 6.8×10^{-14}) obtained from swimming trajectories of SS-5. The data represent the mean value, and errors bars correspond to standard deviation (without GMF: 99.7 ± 1.6 μm/s; with GMF: 115.5 ± 5.5 μm/s).

(B–F) (B) Speed distribution of SS-5 bacteria with few or no magnetosomes in the presence and absence of the GMF. TEM image of a bacterium with no magnetosome (C), with fewer magnetosomes (D) and either deformed (E) or broken (F) magnetosome chains.

(G) Speed distribution of a bacterial suspension subjected to 50 mT magnetic fields to deform or break the magnetosome chain (*t* value: 2.1;: *p* value: 0.8).

The subsequent decrease in speed in the presence of greater than geomagnetic fields is reminiscent of a study by Pan et al.[39] where the magnetic coccoid bacteria MYC-1's migration speed decreased for magnetic fields ranging from 0.1 mT to 1.5 mT. Our results in combination with theirs indicate that magnetotactic bacterial swimming is optimized under field intensities close to that of the geomagnetic field.

Furthermore, the difference in switching rates of the bacterial flagellar motor in the presence and absence of a GMF indicates that the presence of GMF lines provides signaling information to SS-5 bacteria that goes beyond simply providing a passive alignment of the cell body to the field lines. SS-5 bacteria in the presence of a GMF swim preferentially toward the magnetic South pole with fewer switching events, whereas in the absence of a GMF, they explore their environment without any preferential orientation and a greater number of switching events, hence randomizing their search for a more profitable environment. Switching of the bacterial flagellar motor rotational direction typically depends on the phosphorylation of the chemotaxis protein CheY.[40] These results thus suggest that the phosphorylation rate of these proteins is actively tuned by the presence of a magnetic field and are a first hint toward magnetosensing. More precisely,

the motor switching dynamics are sensitive to temporal gradients of magnetic fields. The data presented in Figure 2B shows that the effect of changes in the absolute value of the applied external magnetic field on the rotational speed of the motor of single cells cannot explain the speed increase in the presence of a weak external magnetic field when cells were swimming in three dimensions. Cell to cell variability when looking at single cell motor dynamics is large. Hence, comparison and matching single-cell motor dynamics to 3D swimming trends of a bacterial bulk population can be misleading. When only single-cell motor dynamics are considered however, a clear, statistically relevant difference in motors' switching rates is observed at the single-cell level when fold changes in an external magnetic field are applied. These results show that bacterial flagellar motor dynamics are sensitive to magnetic field intensities varying over time reminiscent of the Weber-Fechner law, which has been extensively studied in the case of chemotaxis[41] but also for sensory senses such as hearing and tactile sensitivity in humans.[42,43]

The exact mechanism behind this apparent mechanosensing however has yet to be uncovered. The previously discussed experiments were repeated under different LED illumination, and the absence of a pronounced effect in the presence of blue-light and magnetic field shows that no cryptochromes are involved in SS-5's magnetosensing mechanism. To test whether the magnetosome chain itself plays a role in the magnetosensing of SS-5 bacteria, experiments altering the magnetosome or the magnetosome chain were conducted. They resulted in two different bacterial populations exhibiting two different swimming behaviors. One of the populations is able to increase its swimming speed in the presence of a GMF, whereas the other is unable to do so and maintains a low swimming speed despite the presence of a GMF. The first population behaves as native SS-5 bacteria, whereas the other likely corresponds to the two bacterial sub-populations with altered magnetosome chains. Hence, these results imply that the magnetosome chain, more specifically the protein filament anchoring the magnetosomes inside the bacteria, plays an essential role in the magnetic signal transduction. These results correlate with previous work done on the actin-like filament, supporting the magnetosome chain in *Magnetospirillum magneticum* AMB-1.[44] In this work, the actin-like chain was shown to interact with the methyl-accepting chemotaxis like proteins at the cell poles, in close vicinity to the bacterial flagellar motor.[44] Although no precise signal transducing receptors have been identified in SS-5, a similar mechanism could be at play for magnetosensing.

Finally, the speed of the model Alphaproteobacterium *Magnetospirillum gryphiswaldense* MSR-1 was also tracked in the presence and absence of a GMF, and no statistical difference in swimming speeds was measured (Figure S6). These differences in behavior may result from physiological differences between the two bacterial strains. SS-5 has a larger magnetic moment than MSR-1, which might accentuate their response to an external magnetic stimuli. Furthermore, MSR-1 and SS-5 are phylogenetically, morphologically, and physiologically different and evolve in different environments (Table in supplementary information; Figure S7). Within the present work, MSR-1 bacteria were cultivated in homogeneous liquid microaerobic conditions, whereas SS-5 bacteria were grown in an oxygen gradient in semi-solid conditions. These differences in growth conditions might contribute to differences in the decision-making of the bacteria and how they respond to external magnetic stimuli.

Magnetosensing enables SS-5 bacteria to align efficiently with magnetic field lines and enhance their swimming velocity in the presence of physiological fields, highlighting their evolutionary adaptation to natural environmental conditions. Discovered in the sediments of the Salton Sea—a shallow, hypersaline lake in California's Colorado Desert—these bacteria thrive in a dynamic habitat. The lake's dissolved oxygen levels vary dramatically, influenced by seasonal stratification and wind-driven mixing events. In spring and summer, oxygen gradients form, with surface waters reaching up to 20 mg O_2/L while bottom waters often becoming anoxic. Wind events in late summer disrupt stratification, mixing oxygen-depleted waters with the surface and temporarily increasing oxygen levels throughout the column. During these events, dissolved oxygen in the entire water column can exceed 3 mg O_2/L from September to January. Additionally, the Salton Sea's sediments, where SS-5 bacteria reside, are frequently disrupted, with nearly 88% of the sediment surface subject to occasional resuspension due to wind and stratification.[45]

These dynamic environmental conditions underscore the importance of magnetosensing as a survival mechanism, allowing SS-5 bacteria to relocate efficiently to their preferred microaerophilic niches when perturbations occur. For MTB such as SS-5, which rely on specific microaerophilic environments, these disruptions pose a significant challenge. When their preferred oxygen levels are perturbed by mixing events, MTB could utilize their ability to rapidly navigate the altered oxygen gradients. In deeper regions of the lake, oxygen is rapidly consumed, leaving large portions of the lake bottom in persistent hypoxia or anoxia.[46] Their enhanced swimming speed in the presence of the geomagnetic field most likely enables them to efficiently relocate after having been transported by currents to suitable microoxic zones. This adaptive behavior is crucial for their survival in a habitat where oxygen dynamics are frequently destabilized by natural physical processes. These findings, together with previous studies,[47] indicate that magnetotactic bacteria, and in our case SS-5 bacteria, have evolved to maximize their swimming efficiency under natural conditions, specifically in the presence of the Earth's magnetic field.

Limitations of the study

The precise molecular mechanism underlying active magnetic field sensing in SS-5 remains unidentified in this study. Future work should focus on developing genetic tools for SS-5 to enable the creation of targeted mutants, which would allow the roles of specific proteins in magnetosensing to be elucidated.

RESOURCE AVAILABILITY

Lead contact

Requests for further information and resources should be directed to and will be fulfilled by the lead contact, Emilie Gachon (emilie.gachon@cea.fr).

Materials availability

This study did not generate new unique reagents.

Data and code availability

- All data reported in this paper will be shared by the lead contact upon request.
- Codes used in this paper can be found in data.
- Any additional information required to reanalyze the data reported in this paper is available from the lead contact upon request.

ACKNOWLEDGMENTS

The authors would like to acknowledge the support from the French Agence Nationale de la Recherche (ANR), under grant PRCI ANR-20-CE92-0051 (project Manaconv) and from Deutsche Forschungsgemeinschaft (DFG, German Research Foundation – project ID 446142122). We acknowledge the Institut de Radioprotection et de Sûreté Nucléaire (IRSN) at CEA Cadarache for access to the transmission electron microscope Tecnai G2 BioTWIN.

AUTHOR CONTRIBUTIONS

E.G., D.F., and M.S. designed research and analyzed the data. E.G. performed the tracking and tethered-cell experiments and their analysis. M.S., S.G., E.T., and E.R. performed experiments and analyzed data. D.F. performed TEM imaging. C.T.L. analyzed data. S.L. and S.K. designed the simulations. S.L. ran the simulations and performed their analysis. D.F. and M.S. supervised the work. E.G. and D.F. wrote the manuscript that was commented by all authors.

DECLARATION OF INTERESTS

The authors declare no competing interests.

STAR★METHODS

Detailed methods are provided in the online version of this paper and include the following:

- KEY RESOURCES TABLE
- EXPERIMENTAL MODEL AND STUDY PARTICIPANT DETAILS
- METHOD DETAILS
  - Growth of the gammaproteobacterium SS-5
  - Growth of the *Magnetospirillum* MSR-1
  - Sample preparation
  - Studying bacteria under different O_2 concentrations
  - Deforming the magnetosome chain
  - Microscopy platform
  - Two-dimensional tracking
  - Three-dimensional tracking
  - Tethered-cell assay
  - Transmission electron microscopy
  - Theoretical model
  - Exploration of swimmer parameter space using Bayesian inference
- QUANTIFICATION AND STATISTICAL ANALYSIS
  - Student T-test
  - Hartigan's dip test

SUPPLEMENTAL INFORMATION

Supplemental information can be found online at https://doi.org/10.1016/j.isci.2025.113377.

Received: October 30, 2024
Revised: February 4, 2025
Accepted: August 13, 2025
Published: August 19, 2025

REFERENCES

1. Johnsen, S., and Lohmann, K.J. (2005). The physics and neurobiology of magnetoreception. Nat. Rev. Neurosci. *6*, 703–712.
2. Lohmann, K.J., Putman, N.F., and Lohmann, C.M.F. (2012). The magnetic map of hatchling loggerhead sea turtles. Curr. Opin. Neurobiol. *22*, 336–342.
3. Hitomi, K., Okamoto, K., Daiyasu, H., Miyashita, H., Iwai, S., Toh, H., Ishiura, M., and Todo, T. (2000). Bacterial cryptochrome and photolyase: characterization of two photolyase-like genes of synechocystis sp. pcc6803. Nucleic Acids Res. *28*, 2353–2362.
4. Maeda, K., Robinson, A.J., Henbest, K.B., Hogben, H.J., Biskup, T., Ahmad, M., Schleicher, E., Weber, S., Timmel, C.R., and Hore, P.J. (2012). Magnetically sensitive light-induced reactions in cryptochrome are consistent with its proposed role as a magnetoreceptor. Proc. Natl. Acad. Sci. USA *109*, 4774–4779.
5. Guerra, P.A., Gegear, R.J., and Reppert, S.M. (2014). A magnetic compass aids monarch butterfly migration. Nat. Commun. *5*, 4164.
6. Frankel, R.B., Bazylinski, D.A., Johnson, M.S., and Taylor, B.L. (1997). Magneto-aerotaxis in marine coccoid bacteria. Biophys. J. *73*, 994–1000.
7. Bazalova, O., Kvicalova, M., Valkova, T., Slaby, P., Bartos, P., Netusil, R., Tomanova, K., Braeunig, P., Lee, H.-J., Sauman, I., et al. (2016). Cryptochrome 2 mediates directional magnetoreception in cockroaches. Proc. Natl. Acad. Sci. USA *113*, 1660–1665.
8. Begall, S., Červený, J., Neef, J., Vojtěch, O., and Burda, H. (2008). Magnetic alignment in grazing and resting cattle and deer. Proc. Natl. Acad. Sci. USA *105*, 13451–13455.
9. Schüler, D. (2006). Magnetoreception and Magnetosomes in Bacteria, *3* (Springer Science & Business Media).
10. Blakemore, R.P. (1982). Magnetotactic bacteria. Annu. Rev. Microbiol. *36*, 217–238.
11. Oh, I.-T., Kwon, H.-J., Kim, S.-C., Kim, H.-J., Lohmann, K.J., and Chae, K.-S. (2020). Behavioral evidence for geomagnetic imprinting and transgenerational inheritance in fruit flies. Proc. Natl. Acad. Sci. USA *117*, 1216–1222.
12. Mouritsen, H., and Ritz, T. (2005). Magnetoreception and its use in bird navigation. Curr. Opin. Neurobiol. *15*, 406–414.
13. Rodgers, C.T., and Hore, P.J. (2009). Chemical magnetoreception in birds: the radical pair mechanism. Proc. Natl. Acad. Sci. USA *106*, 353–360.
14. Ritz, T., Wiltschko, R., Hore, P.J., Rodgers, C.T., Stapput, K., Thalau, P., Timmel, C.R., and Wiltschko, W. (2009). Magnetic compass of birds is based on a molecule with optimal directional sensitivity. Biophys. J. *96*, 3451–3457.
15. Åkesson, S., Morin, J., Muheim, R., and Ottosson, U. (2001). Avian orientation at steep angles of inclination: experiments with migratory white–crowned sparrows at the magnetic north pole. Proc. R. Soc. B Biol. Sci. *268*, 1907–1913.
16. Schwarze, S., Steenken, F., Thiele, N., Kobylkov, D., Lefeldt, N., Dreyer, D., Schneider, N.-L., and Mouritsen, H. (2016). Migratory blackcaps can use their magnetic compass at 5 degrees inclination, but are completely random at 0 degrees inclination. Sci. Rep. *6*, 33805.
17. Schiffner, I., and Wiltschko, R. (2011). Temporal fluctuations of the geomagnetic field affect pigeons' entire homing flight. J. Comp. Physiol. *197*, 765–772.
18. Zapka, M., Heyers, D., Hein, C.M., Engels, S., Schneider, N.-L., Hans, J., Weiler, S., Dreyer, D., Kishkinev, D., Wild, J.M., and Mouritsen, H. (2009). Visual but not trigeminal mediation of magnetic compass information in a migratory bird. Nature *461*, 1274–1277.
19. Treiber, C.D., Salzer, M.C., Riegler, J., Edelman, N., Sugar, C., Breuss, M., Pichler, P., Cadiou, H., Saunders, M., Lythgoe, M., et al. (2012). Clusters of iron-rich cells in the upper beak of pigeons are macrophages not magnetosensitive neurons. Nature *484*, 367–370.
20. Irwin, W.P., and Lohmann, K.J. (2005). Disruption of magnetic orientation in hatchling loggerhead sea turtles by pulsed magnetic fields. J. Comp. Physiol. *191*, 475–480.

21. Cranfield, C.G., Dawe, A., Karloukovski, V., Dunin-Borkowski, R.E., De Pomerai, D., and Dobson, J. (2004). Biogenic magnetite in the nematode caenorhabditis elegans. Proc. Biol. Sci. *271*, S436–S439.

22. Malkemper, E.P., Pikulik, P., Krause, T.L., Liu, J., Zhang, L., Hamauei, B., and Scholz, M. (2023). C. elegans is not a robust model organism for the magnetic sense. Commun. Biol. *6*, 242.

23. Klumpp, S., Lefèvre, C.T., Bennet, M., and Faivre, D. (2019). Swimming with magnets: from biological organisms to synthetic devices. Phys. Rep. *789*, 1–54.

24. Müller, F.D., Schüler, D., and Pfeiffer, D. (2020). A compass to boost navigation: cell biology of bacterial magnetotaxis. J. Bacteriol. *202*, 10–1128.

25. Popp, F., Armitage, J.P., and Schüler, D. (2014). Polarity of bacterial magnetotaxis is controlled by aerotaxis through a common sensory pathway. Nat. Commun. *5*, 5398.

26. Zhu, X., Ge, X., Li, N., Wu, L.-F., Luo, C., Ouyang, Q., Tu, Y., and Chen, G. (2014). Angle sensing in magnetotaxis of magnetospirillum magneticum amb-1. Integr. Biol. *6*, 706–713.

27. Lefevre, C.T., Viloria, N., Schmidt, M.L., Posfai, M., Frankel, R.B., and Bazylinski, D.A. (2012). Novel magnetite-producing magnetotactic bacteria belonging to the gammaproteobacteria. ISME J. *6*, 440–450.

28. Nogueiral, F.S., and De Barros, H.G.P.L. (1995). Study of the motion of magnetotactic bacteria. Eur. Biophys. J. *24*, 13–21. https://doi.org/10.1007/bf00216826.

29. Reufer, M., Besseling, R., Schwarz-Linek, J., Martinez, V.A., Morozov, A. N., Arlt, J., Trubitsyn, D., Ward, F.B., and Poon, W.C.K. (2014). Switching of swimming modes in magnetospirillium gryphiswaldense. Biophys. J. *106*, 37–46.

30. Ērglis, K., Wen, Q., Ose, V., Zeltins, A., Sharipo, A., Janmey, P.A., and Cēbers, A. (2007). Dynamics of magnetotactic bacteria in a rotating magnetic field. Biophys. J. *93*, 1402–1412.

31. Nadkarni, R., Barkley, S., and Fradin, C. (2013). A comparison of methods to measure the magnetic moment of magnetotactic bacteria through analysis of their trajectories in external magnetic fields. PLoS One *8*, e82064.

32. Schulten, K., Swenberg, C.E., and Weller, A. (1978). A biomagnetic sensory mechanism based on magnetic field modulated coherent electron spin motion. Z. Phys. Chem. *111*, 1–5.

33. Steiner, U.E., and Ulrich, T. (1989). Magnetic field effects in chemical kinetics and related phenomena. Chem. Rev. *89*, 51–147.

34. Ritz, T., Adem, S., and Schulten, K. (2000). A model for photoreceptor-based magnetoreception in birds. Biophys. J. *78*, 707–718.

35. Hore, P.J., and Mouritsen, H. (2016). The radical-pair mechanism of magnetoreception. Annu. Rev. Biophys. *45*, 299–344.

36. Xu, J., Jarocha, L.E., Zollitsch, T., Konowalczyk, M., Henbest, K.B., Richert, S., Golesworthy, M.J., Schmidt, J., Déjean, V., Sowood, D.J.C., et al. (2021). Magnetic sensitivity of cryptochrome 4 from a migratory songbird. Nature *594*, 535–540.

37. Frankel, R.B., and Bazylinski, D.A. (2006). How magnetotactic bacteria make magnetosomes queue up. Trends Microbiol. *14*, 329–331.

38. Günther, E., Klauß, A., Toro-Nahuelpan, M., Schüler, D., Hille, C., and Faivre, D. (2019). The in vivo mechanics of the magnetotactic backbone as revealed by correlative flim-fret and sted microscopy. Sci. Rep. *9*, 19615.

39. Pan, Y., Lin, W., Li, J., Wu, W., Tian, L., Deng, C., Liu, Q., Zhu, R., Winklhofer, M., and Petersen, N. (2009). Reduced efficiency of magnetotaxis in magnetotactic coccoid bacteria in higher than geomagnetic fields. Biophys. J. *97*, 986–991.

40. Ma, Q., Sowa, Y., Baker, M.A.B., and Bai, F. (2016). Bacterial flagellar motor switch in response to chey-p regulation and motor structural alterations. Biophys. J. *110*, 1411–1420.

41. Mesibov, R., Ordal, G.W., and Adler, J. (1973). The range of attractant concentrations for bacterial chemotaxis and the threshold and size of response over this range: Weber law and related phenomena. J. Gen. Physiol. *62*, 203–223.

42. Zeng, F.-G. (2020). A unified theory of psychophysical laws in auditory intensity perception. Front. Psychol. *11*, 1459.

43. Nicolas, S. (2017). Weber's compass and the measurement of the threshold of tactile sensitivity: Alfred binet's critical approach to esthesiometry. Annee Psychol. *117*, 41–43.

44. Philippe, N., and Wu, L.-F. (2010). An mcp-like protein interacts with the mamk cytoskeleton and is involved in magnetotaxis in magnetospirillum magneticum amb-1. J. Mol. Biol. *400*, 309–322.

45. Anderson, M., Whiteaker, L., Wakefield, E., and Amrhein, C. (2008). Properties and distribution of sediment in the salton sea, california: an assessment of predictive models. In The Salton Sea Centennial Symposium: Proceedings of a Symposium Celebrating a Century of Symbiosis Among Agriculture, Wildlife and People, 1905–2005, held in San Diego, California, USA, March 2005 (Springer), pp. 97–110.

46. Watts, J.M., Swan, B.K., Tiffany, M.A., and Hurlbert, S.H. (2001). Thermal, mixing, and oxygen regimes of the salton sea, california, 1997–1999. In Saline Lakes: Publications from the 7th International Conference on Salt Lakes, held in Death Valley National Park, California, USA, September 1999 (Springer), pp. 159–176.

47. Codutti, A., Charsooghi, M.A., Marx, K., Cerdá-Doñate, E., Munoz, O., Zaslansky, P., Telezki, V., Robinson, T., Faivre, D., and Klumpp, S. (2023). Escape problem of magnetotactic bacteria-physiological magnetic field strengths help magnetotactic bacteria navigate in simulated sediments. Preprint at bioRxiv. https://doi.org/10.1101/2023.12.08.570788.

48. Bazylinski, D. A., Lefèvre, C. T., and Schüler, D. (2013). Magnetotactic bacteria. In The prokaryotes, E. Rosenberg, E.F. DeLong, S. Lory, E. Stackebrandt, and F. Thompson, eds. (Springer), pp. 453–494.

49. Heyen, U., and Schüler, D. (2003). Growth and magnetosome formation by microaerophilic magnetospirillum strains in an oxygen-controlled fermentor. Appl. Microbiol. Biotechnol. *61*, 536–544.

50. Bennet, M., McCarthy, A., Fix, D., Edwards, M.R., Repp, F., Vach, P., Dunlop, J.W.C., Sitti, M., Buller, G.S., Klumpp, S., and Faivre, D. (2014). Influence of magnetic fields on magneto-aerotaxis. PLoS One *9*, e101150.

51. Barkley, S., Dimiduk, T.G., Fung, J., Kaz, D.M., Manoharan, V.N., McGorty, R., Perry, R.W., and Wang, A. (2020). Holographic microscopy with python and holopy. Comput. Sci. Eng. *22*, 72–82. https://doi.org/10.1109/MCSE.2019.2923974.

52. Deckel, Y., Lowe, L.A., Rawat, S., Turner, M., Luong, J., and Wang, A. (2023). Using holographic microscopy to measure the effect of confinement on crowding agents in lipid vesicles. Chembiochem *24*, e202300069.

53. Boyle, M. (2017). The integration of angular velocity. Adv. Appl. Clifford Algebr. *27*, 2345–2374. https://doi.org/10.1007/s00006-017-0793-z.

54. von Toussaint, U. (2011). Bayesian inference in physics. Rev. Mod. Phys. *83*, 943–999. https://doi.org/10.1103/RevModPhys.83.943.

55. Klumpp, S., Lefèvre, C.T., Bennet, M., and Faivre, D. (2019). Swimming with magnets: From biological organisms to synthetic devices. Phys. Rep. *789*, 1–54. https://doi.org/10.1016/j.physrep.2018.10.007.

56. Thiébaux, H.J., and Zwiers, F.W. (1984). The Interpretation and Estimation of Effective Sample Size. J. Appl. Meteorol. Climatol. *23*, 800–811. https://doi.org/10.1175/1520-0450(1984)023<0800:TIAEOE>2.0.CO;2.

57. Hartigan, J.A., and Hartigan, P.M. (1985). The dip test of unimodality. Ann. Stat. *13*, 70–84.

STAR★METHODS

KEY RESOURCES TABLE

REAGENT or RESOURCE	SOURCE	IDENTIFIER
Antibodies		
Biotin Anti-Flagellin antibody	Abcam	ab193301
Bacterial and virus strains		
Magnetospirillum gryphiswaldense	N/A	GCA_002995515
Gammaproteobacterium SS-5	N/A	N/A
Chemicals, peptides, and recombinant proteins		
Agarose, Low melting	https://www.sigmaaldrich.com/FR/fr/product/mm/2070op	CAS: 9012-36-6
Deposited data		
Raw and analyzed data	This paper	ISCIENCE-D-24-14011R1
Software and algorithms		
Python version 3.9.12	Python Software Foundation	https://www.python.org
Bacteria rotation analysis software	BRAS software	https://bras.sourceforge.net/intro.html
Trackpy 0.6.4	Trackpy: Fast, Flexible Particle-Tracking Toolkit	https://soft-matter.github.io/trackpy/v0.6.4/
HoloPy 3.5.0	Holography and Light Scattering in Python	https://holopy.readthedocs.io/en/master/
Code for simulation		https://doi.org/10.25625/ZQYX5R

EXPERIMENTAL MODEL AND STUDY PARTICIPANT DETAILS

This study involved two magnetotactic bacterial strains: *Magnetospirillum gryphiswaldense* MSR-1 and the *gammaproteobacterium* SS-5. Both strains are prokaryotic microbial models, maintained and cultured under microaerobic conditions at 28°C in defined media (see subsections "growth of the gammaproteobacterium SS-5" and "growth of the *Magnetospirillum* MSR-1") optimized for their growth and magnetosome production.

METHOD DETAILS

Growth of the gammaproteobacterium SS-5

Bacteria were grown in an oxygen-gradient hypersaline medium[48] in autotrophic conditions using thiosulfate as the electron donor and $NaHCO_3$ as the carbon source. The medium routinely contained 31.8 μM of iron, or when specified, 1.8 μM of iron, corresponding to low-iron conditions. Bacterial cultures were inoculated at 1:100 to 1:200 dilutions from one week-old pre-cultures. Bacterial behaviors were studied with one week-old cells after at least three sub-culturing in identical conditions.

Growth of the *Magnetospirillum* MSR-1

MSR-1 cultures were grown in Flask Standard Medium (FSM) as described in Hayen and Schuler in 15 mL falcon tubes with a 1 mL headspace.[49] The cultures were inoculated with 300 μL of a stationnary phase pre-culture and grown to semi-exponential phase. 1 mL of the cell suspension was collected and centrifuged at 1200 RCF for 10 min and resuspended in FSM to obtain an optical density of 0.2 at 600 nm.

Sample preparation

Studying SS-5 under homogeneous conditions requires the extraction of the cells from their semi-solid growth media. 1 mL of growth media was centrifuged for 10 min at 21,583 × g. After centrifugation, the agarose formed a pellet at the bottom of the Eppendorf tube and the overlaying liquid media was harvested. A 500 μL drop of the liquid media was placed a couple of millimeters away from a 500 μL drop of cell suspension on a piece of Parafilm .

Using a pipette tip, the two drops were then put in contact to form a single drop with two distinct phases: a semi-solid one and a liquid one. Two bar magnets (Figure 5B) were used to force North-seeking cells from the semi-solid phase to the liquid phase of the drop. The north pole of a magnet was positioned by the semi-solid phase of the drop whereas the south pole of a second magnet was positioned toward the liquid phase of the drop.

Magnetically aided migration of the cells into the liquid phase of the media was done for 30 min to ensure that a high enough concentration of cells would be in the liquid phase. The liquid phase, containing the North-seeking bacteria was then collected and placed in a 1.5 mL Eppendorf .

Samples were then prepared by cutting a 1 cm hole inside a square piece of 200 μm thick double-sided tape. The tape was stuck to a glass microscope slide. 40 μL of the liquid cell suspension was placed inside the hole and a coverslip was placed on top and in contact with the tape to seal the cell suspension inside a 200 μm thick chamber.

Studying bacteria under different O_2 concentrations

The extraction of the cells from their semi-solid environment occurs under ambient conditions i.e., at roughly 21% of O_2 content. To study cells at a low O_2 concentration, at least 200 μL of the liquid cell suspension was placed in an Eppendorf tube. The top of the tube was pierced by two syringe needles. One was placed inside the cell suspension whereas the second one was placed in the head space of the tube. The needle inside the cell suspension was connected to the gas ramp and N_2 was flushed into the media for 5 min. The second needle allowed the dissipation of gases to prevent over pressurisation inside the tubE.

After the 5 min the needles were taken out of the tube and the holes were sealed with tape. Samples were then prepared was described in section sample preparation.

Deforming the magnetosome chain

A 60 μL drop of bacterial suspension, which were embedded in a 0.2% semi-solid growth media were deposited on a glass slide. 500 μL of a 1.4% low-melting agarose gel from Sigma-Aldrich was added on top of the bacterial suspension drop. The bacteria were then embedded in a 1.2% low-melting agarose gel. The microscope slide was placed on the magnetic microscope stage where a 1 mT field in the x-direction was applied which aligned the bacteria as the gel cooled and solidified around them. An aluminum plate with a pair of permanent magnets (magnetic field strength: 50 mT) was placed on top of the microscope slide. The bacterial suspension in a gel was placed in the center of the aluminum plate such that the magnets did not touch it, with both magnets on either side of the drop. The aluminum plate was rotated 50 times and maintained in place such that the magnetic field was perpendicular to the cell alignment for 5 min. The cells in the 1.2% gel were then collected and placed in a 2 mL Eppendorf tube with 1.3 mL of liquid growth media previously heated to 60°C. The Eppendorf tube was placed in 38°C bath for 15 min.

500 μL of the cell suspension was then collected and the cells were forced to migrate toward a liquid media drop as described in the section sample preparation. This cell suspension was used to both image the cells as described in the section Microscopy set-up and tracking of bacteria and to make transmission electron microscopy grids.

Microscopy platform

A custom-made inverted microscope was built on a non-magnetic, aluminum, platform upon which are set-up three pairs of Helmholtz coils and which also accomodates two light sources and a camera (Zyla from Andor). The illumination source for brightfield imaging is a pE-100, 585 nm wavelength LED from CoolLeD Ltd. The microscope is capable of fluorescence imaging in an epifluorescence inverted mode with a single excitation source the pE-4000 LED 16 LED illumination system from CoolLed Ltd. For the purpose of this study, no fluorescence imaging was done but the epifluorescence illumination system was used to shine different wavelegnths (470 nm, 635 nm, and 740 nm) at the sample.

The triaxial Helmoholtz coil-set and controller (C-SpinCoil-XYZ, Micro Magnetics Inc.) were used to generate DC magnetic fields. Using this set-up five different magnetic conditions were applied to the samples under using a LabView based program (LabView, National Instruments). The first was canceling of the Earth's magnetic field. The magnetic field coordinates in the precise location of our laboratory were obtained from the National Centers Environmental Information's website (https://www.ngdc.noaa.gov/geomag/magfield.shtml). The opposing coordinates were then fed into the LabView program to cancel the ambient field. The magnetic field was then set to 0 μT, 50 μT, 500 μT or 1 mT either along the z axis or the x axis.[50]

Two-dimensional tracking

Videos of bacteria were acquired with a 20× Nikon objective at 40 fps. Two dimensional tracking of MSR-1 bacteria was achieved with a Python code suing the TrackPy package. User inputs for particle size, referring to the (estimated) size of the bacteria in pixels was set to 11 and the minimum mass, referring to the total integrated brightness within the pixels representing the bacterial area was set to roughly 150. Trajectories that lasted less than 5 s were filtered out. Once the trajectories of all the bacteria in the video were obtained the speed of each bacteria was calculated using the following equation:

$$v(x,y)_i = \left(\frac{\sqrt{(x_{i+1} - x_i)^2 + (y_{i+1} - y_i)^2}}{t_{i+1} - t_i} \right) \quad \text{(Equation 1)}$$

The instantaneous speed between frames was calculated for each trajectory, then averaged to obtain its mean speed. The trajectory averages were then combined to determine the bacteria's overall average speed under a given condition.

Three-dimensional tracking

Videos of bacteria were acquired with a 20× Nikon objective at 40 fps. Three-dimensional tracking of SS-5 bacteria was done using holography. A polarizer was placed before the brightfield illumination source. A custom-built Python code, which allows the user to select a region of interest (ROI) around the bacteria was used to track this ROI in all the frames as the bacteria moved and obtain its two dimensional trajectory in the (x,y) plane. To obtain the z coordinates of the bacteria, the ROI in all of the frames of the video is saved as a separate video. Each frame of the video of the ROI is then compared to a library of simulated holograms which represents the holograms one could expect to obtain for different z-coordinates of the bacteria.[51,52] These holograms were constructed using the HoloPy library in Python from an image of an SS-5 stuck to the microscope slide. The comparison is done by calculating the root-mean-square error, RMSE, between the simulated holograms and the frames of the video (Equation 2).

$$\sqrt{\frac{1}{n}\Sigma_{i=1}^{n}(S_i - F_i)^2} \quad \text{(Equation 2)}$$

where S_i corresponds to the simulated holograms, F_i corresponds to the frames of the video and n corresponds to the number of simulated holograms.

The RMSE for a single frame compared to all of the simulated holograms is then plotted and smoothed. The simulated hologram which generates the smallest RMSE value with the studied frame gives the user the approximate position in z of the bacteria. Trajectories that lasted less than 5 s were discarded and the speed of the bacteria from the remaining trajectories was calculated as follows:

$$v(x,y,z)_i = \left(\frac{\sqrt{(x_{i+1} - x_i)^2 + (y_{i+1} - y_i)^2 + (z_{i+1} - z_i)^2}}{t_{i+1} - t_i}\right) \quad \text{(Equation 3)}$$

The instantaneous speed between frames was calculated for each trajectory, then averaged to obtain its mean speed. The trajectory averages were then combined to determine the bacteria's overall average speed under a given condition.

Tethered-cell assay

Thethered cell-assays were done by letting the SS-5 bacteria sediment to the bottom of the 200 μm thick sample chamber in the presence of an external 1 mT Z-field. By applying a field in the z direction (perpendicular to the glass slide), the cells oriented their bodies such that some sedimented with the flagella positioned toward the bottom coverslip. By attaching to the coverslip with their flagella, the bacterial flagellar motor forced the rotation of the cell body.

Similarly, MSR-1 tethered-bead assays were done by first shearing off part part of MSR-1 bacteria's flagella by transferring the cell suspension into a 1 mL syringe and attaching a 23 G needle to the end. The needle was then connected to a polyethylene tubing with an inner diameter of 0.56 mm. the other end of the tubing was attached to another needle and empty syringe. The cell suspension was passed back forth from one syringe to the other fifty times. The flagellas are very fragile and break off easily. The cell suspension was then centrifuged three times at 4000 G and resuspended every single time in an equal volume of FSM. 200 μ L of the cell suspension was then incubated on ice with a 10 μ L of a 1/50 dilution of an anti-fliC-biotin antibody (Abcam) for 5 min. The cell suspension is then placed on a microscope slide and the sample is prepared as described in sample preparation. After a few minutes, flagella are stuck to the microscope slide and rotating cell bodies can be observed.

The tracking of the cells was done by using the open source Bacterial Rotation Analysis Software (BRAS, www.bras.sourceforge.net). The (x,y) coordinates were then used as inputs in a custom-built Python code, which corrected for any drift of the cell and calculated the bacteria's motor rotational speed.

Transmission electron microscopy

TEM was used to compare magnetosome organization in the different bacterial samples (low iron concentration, mechanical treatment to deform the chain, control condition). Cells were directly deposited onto TEM copper grids coated with a carbon film. Electron micrographs were recorded with a Tecnai G2 BioTWIN (FEI) equipped with a CCD camera (Megaview III, Olympus Soft imaging Solutions GmbH) with an accelerating voltage of 100 kV.

Theoretical model

For simulations of the swimming of SS-5, we used a model equivalent to the one described in Nogueiral and De Barros.[28] The bacterium is described as a spherical swimmer of radius R with translational diffusion constant $D = k_BT/6\pi\eta R$ and rotational diffusion constant $D_R = k_BT/8\pi\eta R^3$ that is propelled by a force of strength $F = v/\mu$, which represents the driving by the flagellum. v is the active instantaneous velocity of the swimmer, and $\mu = D/k_BT$ is the translational mobility. In the coordinate system of the swimmer, the force is given by $\overrightarrow{F}(t) = v/\mu\cdot(\cos(\alpha), \sin(\alpha)\cos(2\pi ft), \sin(\alpha)\sin(2\pi ft))^T$, rotating at with frequency $f = 200Hz$ around the local x axis. The *force angle* α between the x axis and the force vector controls the amount of helicity the resulting trajectory shows. The force acts upon the rear end $A = (-R, 0, 0)^T$ of the swimmer, leading to a torque $\tau_A(t) = A \times F(t)$ on the swimmer. Additionally, the motor produces a torque $\tau_M = -2\pi f_S/\mu_R$ around the flagellar axis (1,0,0). Here, $f_S = f/2$ is the speed at which the swimmer rotates around

its local x axis in response to the applied torque, and $\mu_R = D_R/k_BT$ is the rotational mobility. We assume that the mobility of the swimmer and the flagellum are equal, and thus, the global rotation is split equally between the two mechanical components. The magnetic dipole moment is assumed to be aligned with the local x axis, leading to the dipole moment $\vec{m} = (m,0,0)^T$.

We describe the global orientation of the swimmer with a quaternion q.[53] It transforms a local torque τ to the lab coordinates via $\tau' = q\tau q^{-1}$. It is also used to transform the dipole moment to the global coordinate system via. We assume the magnetic field of strength B to be aligned with the global x axis, leading to a magnetic torque of $\vec{\tau}'_B = \vec{m}' \times (B,0,0)^T$. The total torque is given by $\vec{\tau}' = \vec{\tau}'_A + \vec{\tau}'_M + \vec{\tau}'_B$. The swimmer's instantaneous angular velocity is given by $\vec{\omega} = \vec{\tau}'\mu_R + \sqrt{2D_R}\vec{\xi}$, with rotational diffusion described by the white noise $\vec{\xi}$ with $\langle\xi_i(t)\rangle = 0$ and $\langle\xi_i(t)\xi_j(t')\rangle = \delta_{ij}\delta(t - t')$. With this, the equation of motion for the swimmer's orientation is given by $dq/dt = 1/2\vec{\omega}q$. The global location $\vec{x}$ of the swimmer evolves as $d\vec{x}/dt = \mu F'(t,q(t)) + \sqrt{2D}\vec{\zeta}$ with white noise $\vec{\zeta}$. The equations of motion are integrated using an Euler-Maruyama discretization. The orientation q is normalized after each time step to maintain numerical stability.

We control the time step Δt of the integration by limiting the quantity $|\vec{\omega}\cdot\Delta t| < 0.1$. This ensures that any rotation is sufficiently resolved and prevents numerical oscillations. The simulation is sampled at precisely 40 Hz, which matches the framerate at which the experimental footage was acquired. The active velocity v is tuned in a separate pilot run without the magnetic field turned on to achieve the desired effective velocity $v_{eff} = 50\mu m/s$ between two observations. The pilot run also produces the initial conditions for the trajectory samples. We let the system equilibrate for $t_P = 5/D_R$, a multiple of the timescale of the rotational diffusion, before sampling the actual trajectories.

Our model has three unknown parameters: the magnetic dipole moment m, the angle α at which the force acts upon the swimmer, and its radius R. We ran an extensive suite of simulations over this parameter space in the physically plausible regions. To this extent, we performed a Bayesian analysis of the parameters. Using the experimental and the simulated distributions of movement directions, we evaluated the likelihood of the parameter triplets and determined their posterior distribution, which indicates the ability of the model to reproduce the experimental data.

Exploration of swimmer parameter space using Bayesian inference

To relate the simulations to the experiments, we used a Bayesian approach.[54] This analysis identifies the parameters of the model that are most plausible in light of experimental evidence and constructs the posterior distribution of the parameters, which can be interpreted as the region of parameters that are most likely to reproduce the measurements. A common measurement must connect the experiment and the generative model (the simulations) for the Bayesian analysis. Here, we linked the experiment to the simulations via the observed angle distribution between the trajectory segments and the magnetic field lines (compare Figure 3A). Note that this quantity is inherently related to the measurement process and depends on the frequency at which the bacterium's location (experimental and simulated) is obtained. Therefore the experiment and the simulation were handled in exactly the same way to avoid a bias. A higher measurement frequency can nonetheless decrease the width of the posterior as more information is gathered and incorporated into the posterior knowledge.

We assumed the angle φ between the trajectory segments and magnetic field to be von Mises-Fisher (MF) distributed[55] in two dimensions. We saw good correspondence between our simulations and the distributions and used it primarily for performance. (The analysis can also be conducted using sampling distributions if MF poorly describes the angles). The density of the MF distribution is

$$p_\kappa(\varphi) = \frac{\kappa}{2\pi I_0(\kappa)} \exp(\kappa\cos\varphi). \quad \text{(Equation 4)}$$

In this expression, I_0 denotes the modified Bessel function of order 0. Note that the localization constant κ does not directly relate to a physical quantity of the swimmer, as this is the trajectory segment orientation, not the true orientation of the swimmer.

The simulation was parametrized by the force angle α, the magnetic dipole moment m, and the radius R of the swimmer. We will refer to a triplet of these as the configuration θ. Then, we obtained the model localization κ_θ by fitting an MF distribution to samples of the simulation under θ. We used 1000 trajectories of length 5 s, sampled at 40 Hz, to obtain the localization.

The experimental data shows substantial heterogeneity (see Figure S2 in supplementary information). In particular, parts of the trajectories appears to move in opposite directions of the magnetic field, which could not be removed by globally filtering out trajectories that move away from the south pole. To obtain the relevant angular distribution, we employed a mixture model

$$p(\varphi) = rp_{\kappa_1}(\varphi + \varphi_1) + (1 - r)p_{\kappa_2}(\varphi + \varphi_2) \quad \text{(Equation 5)}$$

of two MF distributions. A maximum-likelihood fit produced an angular offset of $\varphi_1 - \varphi_2 = 151^\circ$ and a mixture ratio of $r = 0.503$. The localization of the large peak is $\kappa_E = 9.242$, which we used for the Bayesian analysis. Finally, we estimated the number of samples available from p_{κ_E} using the time series of the experimental trajectories. We calculated the estimated sample size (ESS),[56] which corrects for the temporal correlations in the time series to obtain the equivalent number of samples if they were obtained independently.

We ignored trajectories that produce ESS < 50, as the ESS calculation is considered unreliable in these situations. From 20899 angles from the experimental data, we determined an ESS of 1950 from the mixture, and therefore, given the mixture ratio r, the equivalent of $N = 981$ independent samples available from the subpopulation moving toward the south pole.

To obtain the posterior distribution $p(\theta|\kappa_E, N) \propto L \cdot p(\theta)$ of the model configurations θ, i.e., to learn which parameter regions best describe the experimental findings κ_E and N, we calculated the *likelihood* $L = p(\kappa_E, N|\theta)$ of the experimental data under the model configuration as follows: We started with the probability of an (experimental) angle φ under an MF distribution described by localization κ_θ: $p_\theta = \frac{1}{2\pi I_0(\kappa_\theta)} e^{\kappa_\theta \cos(\varphi)}$ The log likelihood $\log p_\theta = -\log(2\pi) - \log I_0(\kappa_\theta) + \kappa_\theta \cos(\varphi)$ is easier to handle analytically than p_θ directly and required for numerical treatment. We thus calculated the expected value of the log likelihood under the assumption that the angle φ is obtained from an experiment that is described by localization κ_E:

$$\mathbb{E}_{\kappa_E}[\log p_\theta] = -\log(2\pi) - \log I_0(\kappa_\theta) + \mathbb{E}_{\kappa_E}[\kappa_\theta \cos \varphi]$$

Using $\mathbb{E}_{\kappa_E}[\kappa_\theta \cos \theta] = \kappa_\theta \mathbb{E}_{\kappa_E}[\cos \theta]$ and,

$$\mathbb{E}_{\kappa_E}[\cos \varphi] = \frac{\int_0^{2\pi} \cos \varphi e^{\kappa_E \cos \varphi} d\varphi}{\int_0^{2\pi} e^{\kappa_E \cos \theta} d\varphi} = \frac{I_1(\kappa_E)}{I_0(\kappa_E)}$$

with the modified Bessel functions I_0 and I_1, we obtained the expected likelihood for a single experimental observation θ as

$$\mathbb{E}_{\kappa_E}[\log p_\theta] = -\log(2\pi) - \log I_0(\kappa_\theta) + \kappa_\theta \frac{I_1(\kappa_E)}{I_0(\kappa_E)}.$$

The log likelihood of N individually independent samples $\varphi_i \sim p_{\kappa_E}$ is therefore,

$$\log p(\kappa_E, N|\theta) = -N \log(2\pi) - N \log(I_0(\kappa_\theta)) + N\kappa_\theta \frac{I_1(\kappa_E)}{I_0(\kappa_E)}. \quad \text{(Equation 6)}$$

The prior $p(\theta)$ defines the knowledge about the parameters before incorporating the experimental evidence. We used a uniform distribution that caps off the radius at $R_{max} = 2\mu m$, the maximum force angle at $\alpha_{max} = 85^\circ$ and the dipole moment $m_{max} = 2.0 \times 10^{-16} Am^2$. We used the prior and the likelihood to sample from the posterior using an ordinary Metropolis-Hastings sampler.[54] The resulting posterior density is shown in Figure S3 in the supplementary information PDF. We saw no correlation between the particle radius and the force angle. The dipole moment is localized at $9.4 \times 10^{-16} Am^2$ (95% CI $[6.0, 12.8] 10^{-16} Am^2$). We observed correlations with large force angles ($> 40^\circ$) and small radii ($< 0.5\mu m$).

We also collected samples from the difference Δv in effective velocities that occur when turning on the magnetic field during the posterior sampling. This produced samples from $p(\Delta v|\kappa_E, N) = \int_\theta p(\Delta v|\theta) p(\theta|N, \kappa_E)\, d\theta$, the posterior predictive distribution of velocity changes for the plausible parameters (see Figure 3E).

QUANTIFICATION AND STATISTICAL ANALYSIS

Student T-test

For the tethered-cell assays, the exact same motors are probed with exposure to different stimuli. To compare the effects of different stimuli, a paired Student's T-test was performed. The t-value, which is a measure of the size of the difference relative to the variation in the dataset, was calculated as follows:

$$t_p = \frac{\overline{d}}{\sqrt{\frac{s^2}{n}}} \quad \text{(Equation 7)}$$

Where $\overline{d}$ is the mean difference, s^2 is the dataset variance and n is the sample size. The greater the t_p-value, the greater the evidence against the null hypothesis.

For the two- and three-dimensional swimming assays, the statistical effect of different stimuli was calculated using an unpaired Student's t test:

$$t_{up} = \frac{m_1 - m_2}{\sqrt{\frac{s^2}{n_1}} + \sqrt{\frac{s^2}{n_2}}} \quad \text{(Equation 8)}$$

where:

$$s = \frac{\sum (x - m_1)^2 + \sum (x - m_2)^2}{n_1 + n_2 - 2} \quad \text{(Equation 9)}$$

m_1 and m_2 are the means and n_1 and n_2 are the sizes of the two different datasets being compared.

Hartigan's dip test

To test whether a speed distribution fits, a unimodal distribution a Hartigan's dip test was performed. This test measures multimodality in a sample by the maximum difference, over all sample points, between the experimental data distribution, and the unimodal distribution function, which minimizes the maximum difference.[57] Hartigan's dip test was run on our data using the Python package diptest 0.5.2, which yields a *p*-value where the null hypothesis is that the distribution of data points is unimodal.